TABLE 1 Comparison Between the Bragg Wavelengths of the FBG Sensors Measured by the Miniaturized Interrogator Prototype and Those Supplied by the Manufacturer

Sensors	Sensor Wavelength (nm)	Sensor Wavelength Supplied by the Manufacturer (nm)
1	1543.486	1543.52
2	1544.267	1544.30
3	1545.048	1545.06
4	1545.911	1545.90
5	1546.658	1546.66

a Gaussian relationship between the signal intensity and the EDG chip temperature, thus confirming Eq. (6). The measured wavelength values for the five gratings are listed in Table 1 and compared to those provided by the manufacturer. It is noted that the measurement resolution of the interrogator is better than 1 pm as the reading resolution of the EDG chip temperature is better than 0.01°C. It is further observed that the measured wavelengths are in good agreement with those provided by the manufacturer. The small variations in wavelengths can be attributed to environmental disturbances, such as the impact of temperature and strain on the grating. It is well known that Bragg wavelength shifts with temperature at a rate of ~13 pm/°C and strain at a rate of ~1.2 pm/$\mu\varepsilon$ for Bragg wavelength of 1550 nm [12].

The developed interrogator was also used to monitor temperatures. Figure 7 shows the experimental results of such temperature variation and illustrates the performance of the interrogator for temperature measurement. By monitoring the EDG temperature corresponding to the maximum optical power in a dedicated channel (Channel 19 in this case), the FBG temperature sensor can be precisely interrogated.

Through proper design of the EDG and use of current technology, 100 channels or more can be interrogated. Moreover, because of the compactness and light-weight of the interrogator, it is possible to stack several miniaturized interrogators together and increase the interrogator capability beyond the developed device presented here. Thus providing added flexibility and increasing the interrogation capability. We are currently working on employing this technology in an aerospace environment. This device is seen of significant potential in robotics, smart clothing, and security systems application requiring light-weight and compactness.

4. CONCLUSIONS

A miniaturized fiber Bragg grating sensor interrogation device based on integrated EDG has been proposed, developed, and prototyped. Results, employing this device, illustrated its performance for temperature measurement and for FBG sensor Bragg wavelength identification. This device is also able to monitor multiFBG sensors simultaneously with a resolution better than 1 pm.

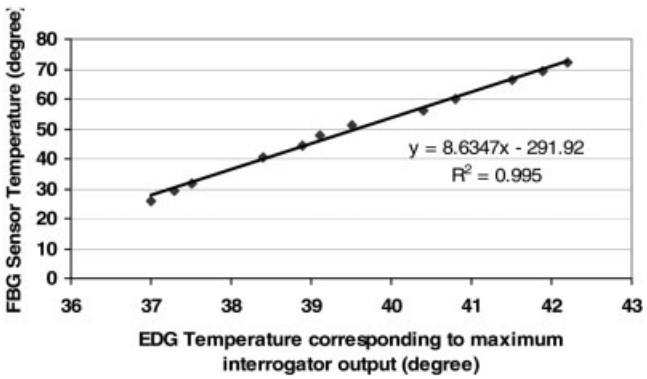

Figure 7 Interrogation result of a FBG temperature sensor using the miniaturized interrogator prototype

REFERENCES

1. J.-R. Lee, C.-Y. Ryu, B.Y. Koo, S.-F. Kang, C.-S. Hong, and C.-Gon Kim, In-flight health monitoring of a subscale wing using a fiber Bragg grating sensor system, Smart Mater Struct 12 (2003), 147–155.
2. K. Wood, T. Brown, R. Rogowski, and B. Jensen, Fiber optic sensors for health monitoring of morphing airframes. I. Bragg gating strain and temperature sensor, Smart Mater Struct 9 (2000), 163–169.
3. S.C. Galea, N. Rajic, I.G. Powlesland, S. Moss, M.J. Konak, S. Van der Velden, A.A. Baker, A.R. Wilson, S.K. Burke, I. McKenzie, Y.L. Koh, and W.K. Chiu, Overview of DSTO smart structures activities related to structural health monitoring, HUMS 2001-DSTO International Conference on Health and Usage Monitoring, Melbourne, February 19–20, 2001.
4. N. Mrad and G.Z. Xiao, Multiplexed fibre Bragg gratings for potential aerospace applications, The 2005 International Conference on MEMS, NANO, and Smart Systems, Banff, Alberta, Canada, July 24–27, 2005. pp. 359–363.
5. http://www.dodsbir.net/sitis/archives_display_topic.asp?Bookmark=27930.
6. A.B.L. Ribeiro, L.A. Ferreira, J.L. Santos, and D.A. Jackson, Analysis of the reflective-matched fiber Bragg grating sensing interrogation scheme, Appl Opt 36 (1997), 934–939.
7. J.J. He, B. Lamontagne, A. Delage, L. Erickson, M. Davies, and E.S. Koteles, Monolithic integrated wavelength demultiplexer based on a waveguide rowland circle grating in InGaAsP/InP, J Lightwave Technol 16 (1998), 631–638.
8. D.A. Jackson, A.B. Lobo Riberio, L. Reeckie, and J.L. Archambault, Simple multiplexing scheme for a fiber-optic grating sensor network, Opt Lett 18 (1993), 1192–1194.
9. G.Z. Xiao, P. Zhao, F.G. Sun, Z.G. Lu, Z. Zhang, and C.P. Grover, Interrogating fiber Bragg grating sensors by thermally scanning an arrayed waveguide grating based demultiplexer, Opt Lett 29 (2004), 2222–2224.
10. Y. Sano and T. Yoshino, Fast optical wavelength interrogator employing arrayed waveguide grating for distributed fiber Bragg grating sensors, J Lightwave Technol 21 (2003), 132–139.
11. V.I. Tolstikhin, A. Densmore, K. Pimenov, Y. Logvin, F. Wu, S. Laframboise, and S. Grabtchak, Monolithically integrated optical channel monitor for DWDM transmission systems, J Lightwave Technol 22 (2004), 146–153.
12. Y.-J. Rao, Fiber Bragg grating sensors: Principles and applications, In: K.T.V. Grattan and B.T. Meggitt (Eds.), Optical fiber sensor technology, Vol. 2, Chapman & Hall, London, 1998, pp. 355–389.

A HYPERBOLIC SUMMATION METHOD TO FOCUS B-SCAN GROUND PENETRATING RADAR IMAGES: AN EXPERIMENTAL STUDY WITH A STEPPED FREQUENCY SYSTEM

Caner Ozdemir,[1] Sevket Demirci,[1] Enes Yigit,[1] and Adnan Kavak[2]
[1] Department of Electrical-Electronics Engineering, Mersin University, Ciftlikkoy, Mersin 33343, Turkey
[2] Department of Computer Engineering, Kocaeli University, Izmit, Kocaeli 41040, Turkey

Received 1 August 2006

ABSTRACT: *There are many techniques to focus raw B-scan ground penetrating radar (GPR) images mainly distorted from well-known hy-*

perbolic dispersion. In this study, we apply a hyperbolic summation (HS)-type focusing technique to the simulated and measured GPR data at C-band frequencies. The formulation of the proposed HS method is presented. Numerical GPR images for different metal targets are generated by the help of a physical optics simulation code. An experimental set-up is constructed with the help of a stepped frequency radar system and corresponding B-scan images are generated. Proposed HS method is applied to the measured B-scan GPR data. Focused GPR images of different objects were obtained for both the simulated and the experimental data. © 2007 Wiley Periodicals, Inc. Microwave Opt Technol Lett 49: 671–676, 2007; Published online in Wiley InterScience (www.interscience.wiley.com). DOI 10.1002/mop.22230

Key words: *inversion; radar imaging; ground penetrating radar; hyperbolic summation*

1. INTRODUCTION

Ground penetrating radar (GPR) is an important remote sensing tool mainly used to detect and image subsurface objects [1–4]. A typical B-scan GPR system collects reflectivity of the subsurface objects when the radar is moving on top of the ground surface and looking downward [5–7]. For the monostatic arrangement, a single point scatterer appears as a hyperbolic parabola in the space-time GPR image when the radar moves along a synthetic aperture. Such an image construct is sometimes satisfactory if the goal is just to detect a pipe or a similar object. However, highly accurate information about the depth, size, and electromagnetic (EM) reflectivity of the buried object(s) is necessary in most GPR applications. Maintenance operations on ancient buildings or stone masonry structures and identification of landmines in humanitarian demining are only a few examples among many in which a high resolution image of the buried objects is very important. If this is the case, then the hyperbolic behavior in the space-time GPR image is often desired to be transformed to a focused pattern that shows the object's true location and size together with its EM scattering. For this purpose, many image focusing algorithms have been developed recently [8–11]. Fisher et al. [8] applied reverse-time migration algorithm for GPR profiles. Capineri et al. [9] employed a Hough transformation technique to the B-scan data to acquire better resolved images of buried pipes. Leuschen and Plumb [10] and Morrow and Van Genderen [11] implemented back-propagation techniques based on finite difference time-domain (FDTD) reverse-time migration algorithms to solve the focusing problem for B-scan GPR images. Beside these algorithms, a simple but an effective method to focus such hyperbolas is the hyperbolic summation (HS) technique that has been successfully applied especially in seismic applications [12, 13]. In this study, we propose a focusing method based on HS technique to the C-band GPR data collected via B-scan processing. The details of our method are presented in Section 2. In the next section, we first apply our focusing algorithm to the numerically generated GPR data obtained for various buried objects such as plates and pipes. Then, we collect measured B-scan GPR data via an experimental set-up with a stepped frequency radar system (SFRS). The real, classical B-scan GPR images were generated and the proposed method is applied to these measurement data and the resultant focused GPR images are presented accordingly. In the last section, the work is summarized and issues regarding the effectiveness and the limitations of the method are discussed.

2. THE FOCUSING METHOD

A typical GPR system collects EM reflectivity of the subsurface objects together with various cluttering effects caused mostly by air-to-ground interface and inhomogeneities within the ground medium [1]. For homogeneous mediums, the phase of the received signal is directly proportional to the trip distance that EM wave possesses. Therefore, the back-scattered signal from a point-scatterer experiences different round-trip distances while the radar is moving along a straight line for the monostatic arrangement as depicted in Figure 1(a). For each discrete point on this aperture, the backscattered signal can be collected within a frequency bandwidth (A-scan process) with the help of a SFRS such that one-dimensional (1-D) range-profile can be acquired by taking the inverse Fourier transform (IFT) of this frequency-diverse data. Then, one can easily construct a 2-D B-scan GPR image in the spatial-time domain by putting all range profiles side by side. After applying these procedures, a point-scatterer shows up as a hyperbolic parabola in this 2-D B-scan GPR image [1, 2]. The shape of this hyperbola depends on the depth of the buried object, the beam-width of the radar antenna, and the relative electric permittivity of the ground medium. The true location of the object is in fact at the top of this hyperbola. Therefore, our ultimate aim is to transform the hyperbolic behaviors on the 2-D B-scan GPR image to focused or at least concentrated patterns with the below methodology that can be considered as a modified version of well known HS technique. While applying the algorithm, we assume that the radar antenna is put very close to air–ground surface and the ground medium is homogeneous as well. These assumptions assures that spatial-time GPR data can easily be converted to

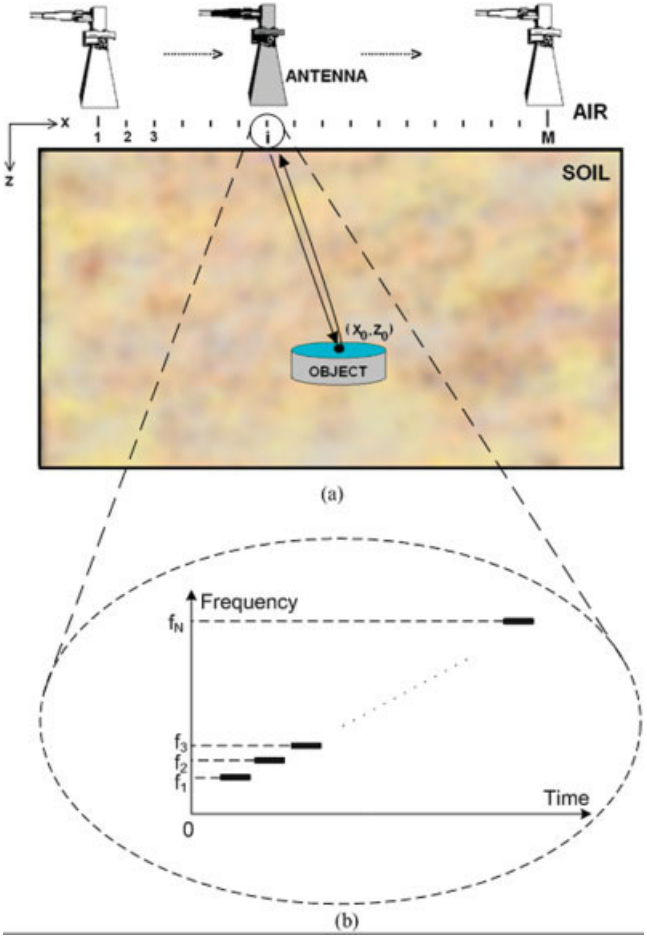

Figure 1 (a) Geometry for the monostatic B-scan GPR problem. (b) At each spatial point, the backscattered signal is collected with equal frequency steps to get a 2-D B-scan data. [Color figure can be viewed in the online issue, which is available at www.interscience.wiley.com]

spatial-spatial GPR data by applying $z = vt$, where v is the velocity of the EM wave inside the ground medium, t is time, and z is the depth-axis. Under these assumptions, therefore, the backscattered electric field from a point scatterer buried at z_0 for an A-scan process can be simply written as

$$E_s(k) = A \exp[-jk(2z_0)], \tag{1}$$

where A is the complex EM scattering value of the buried scatterer and k is the wave-number inside the ground. It is obvious that $k = k_0\sqrt{\varepsilon_r}$, where k_0 is the wave-number in vacuum and ε_r is the dielectric constant of the ground.

Our method can be summarized as follows: (i) The scattered field from subsurface environment is collected along a straight path via SFR set-up such that the frequency is varied within a certain bandwidth of f_{BW} for N equally spaced steps either for monostatic or bistatic configuration [see Fig. 1(b)]. Then, 1-D A-scan depth-profile can be constructed by taking the 1-D inverse Fourier transforming (IFT) of the 1-D frequency data as shown below

$$E_s(z) = \mathrm{IFT}\{E_s(k)\} = A \cdot \mathrm{IFT}_{2k}\{\exp(-j2k(z_0))\} = A \cdot \delta(z - z_0), \tag{2}$$

where $\delta(z - z_0)$ is the impulse function. It is obvious that Ref. 2 indicates a peak of amplitude A, located at $z = z_0$, where the point scatterer actually lies. Similarly, traditional 2-D space-depth B-scan GPR image is obtained by taking the 1-D inverse Fourier transforming (IFT) of the 2-D spatial-frequency data. According to Fourier theory, range (or depth) resolution is given by

$$\Delta z = \frac{2\pi}{2k_{BW}} = \frac{\pi y}{2\pi f_{BW}} = \frac{v}{2f_{BW}}, \tag{3}$$

where k_{BW} is the bandwidth in wave-number domain and v is the speed of light inside the ground medium. For homogeneous and lossless mediums, $v = c/\sqrt{\varepsilon_r}$, where c is the speed of light in vacuum. The depth extend; z_{max} is then can be calculated via

$$z_{max} = N\Delta z = \frac{Nc}{2\sqrt{\varepsilon_r} f_{BW}}. \tag{4}$$

When the radar is moving on a synthetic aperture along a 1-D vector X, a point scatterer located at (x_0, z_0) shows up as a hyperbola whose depth equation can be written as

$$z = \sqrt{z_0^2 + (X - x_0)^2}. \tag{5}$$

Noting that a B-scan GPR image is obtained by the summation of finite number of hyperbolas that correspond to different point scatterers on the buried object(s), it is possible to resolve these points through the following steps. (ii) For each pixel point (x_i, z_i) in the original 2-D B-scan GPR image, we find the hyperbolic template for the synthetic aperture vector X using $z = \sqrt{z_i^2 + (X - x_i)^2}$. (iii) We trace the image data for the pixels under this hyperbolic template. At this point, we have a 1-D data $E_s(x)$ whose length M is the same as the total number of sampling points in X. (iv) Afterward, we calculate the root-mean-square (rms) value of the total energy contained in this 1-D complex image data as

$$\{\text{rms at } (r_i, z_i)\} = \sqrt{\frac{|E_s(x)|^2 |E_s^*(x)|^2}{M}} = \frac{1}{\sqrt{M}} \sum_{m=1}^{M} |E_s(x)|^2. \tag{6}$$

(v) We then record the calculated rms value of the contained energy to the single pixel at (r_i, z_i) in the new 2-D GPR image. Therefore, a hyperbolic behavior in the original image is, in fact, mapped to a single image data point at (r_i, z_i) that contains the summation of the energies under this hyperbolic template in the new image. We successively repeat the same procedure until all the pixels in the original 2-D GPR image are covered.

3. SIMULATION AND MEASUREMENT RESULTS

The validity and the effectiveness of the proposed method are tested via simulated and measured data for various test objects.

3.1. Simulation Results

For the EM calculation of the scattering from buried objects, a physical optics (PO)-based simulator that utilizes the shooting and bouncing ray (SBR) technique is employed [14]. This simulator can successfully estimate EM scattering from metallic targets only for homogeneous mediums [15, 16]. Therefore, air–soil interface is neglected during this simulation assuming that the relative permittivity of the ground medium is not too high. The B-scan GPR geometry shown in Figure 1 is simulated by the help of our PO-SBR-based code. The dielectric constant of the ground is taken as 4.0. The back-scattered EM signature is collected along the synthetic aperture of 1 m in x-direction for a total of 64 discrete spatial points. The frequency is also varied from 6.8187 to 9.1443 GHz such that the back-scattered signal is collected for a total of 64 discrete frequencies at each spatial point. Therefore, a 64-by-64, 2-D spatial-frequency B-scan back-scattered E-field data is gathered.

Two metal pipes and a metal plate with different sizes were located at different locations as the buried objects. The CAD file of these objects is shown in Figure 2(a). A pipe with 12 cm in diameter and 50 cm in length is put horizontally at $x = 20$ cm and $z = 35$ cm. Another pipe with 6 cm in diameter and 30 cm in length is also positioned horizontally at $x = 50$ cm and $z = 25$ cm. The 10 cm $\times$ 10 cm metal plate is buried flat at $x = 75$ cm and $z = 30$ cm. As plotted in Figure 2(b), the traditional GPR image is obtained in spatial-depth domain by taking the 1-D IFFT of the 2-D back-scattered data along the frequency domain. While processing the image, the image matrix is upsampled by applying a four-times zero-padding procedure to get a better resolved image. As expected, the image is defocused hyperbolically due to reasons explained in Section 2. The outlines of the objects are drawn in green for referencing purposes. The image obtained by the proposed method in depicted in Figure 2(c) where the key scattering mechanisms from the top of the pipes and the plate is very well focused. As anticipated, the image of the EM scattering from the flat-plate is dominant although it is buried deeper than the upper pipe. The algorithm works quite fast as well. It took only 53 s to complete the transformation and form this 256-by-256 new image on an IBM-PC with 1.73 GHz processor and a 1 GB of RAM.

3.2. Experimental Results

To obtain real B-scan GPR measurements, we have constructed an experimental set-up with the geometry shown in Figure 3(a). We built a large wooden pool that is filled with homogeneous, dry sand material whose dielectric constant is almost constant around 2.4 between 5 and 8 GHz. We have assembled a frequency stepped continuous radar (FSWR) experimental set-up with the help of

Agilent E5071B ENA vector network analyzer (VNA) and different C-band pyramidal rectangular horn antennas. The measured data from the VNA is recorded to a computer via GPIB port. A typical experiment scene is pictured in Figure 3(b).

To test the algorithm, we conducted a couple of B-scan GPR experiment with the help of our experimental set-up. In the first experiment, a thick iron pipe with 16.5 cm in diameter and 47 cm in length was buried flat at 15 cm below the sand's surface. Under monostatic configuration, the backscattered field data is collected along a synthetic aperture length of 120 cm for a total of 61 discrete spatial points via S_{11} measurements with the help of an AHS-SAS 584 pyramidal rectangular horn antenna. Antenna was located just above the sand's surface and headed toward the buried object while it is moving along the aperture. The VNA's frequency is varied from 4.8 to 8.5 GHz with 18.5-MHz frequency steps such that we measure 201 discrete frequency points for each spatial point. Then, by taking the 1-D IFT of this measured S_{11} data, we obtained the 2-D spatial-depth GPR image as shown in Figure 4(a). Again, the GPR image also exhibits the undesired hyperbolic behavior. The reflection from the sand's surface is easily observed at $z = 0$ cm. The reason that we see a significant reflection from the sand's surface near the object is that the antenna was directed almost downward at those aperture points during the experiment and therefore, a mirror-like backscattering mechanism from the sand surface occurred. During the inversion, the speed of the EM wave was taken as $v = c/\sqrt{2.4}$. Since the antenna is put just above the ground surface, EM wave traveled inside the sand in most of the trip time and so, this turned out to be not a bad approximation as seen from Figure 4(a). In fact, one can observe that the hyperbola in the GPR image makes a peak around $z = 15$ cm, which is the exact location of the pipe. After applying our HS focusing algorithm, we formed the new GPR image as shown in Figure 4(b). As seen from the figure, new image well focused at the true location of the key scattering from subsurface environment.

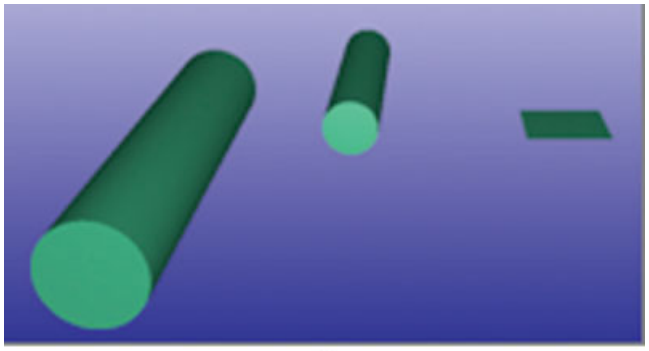

(a)

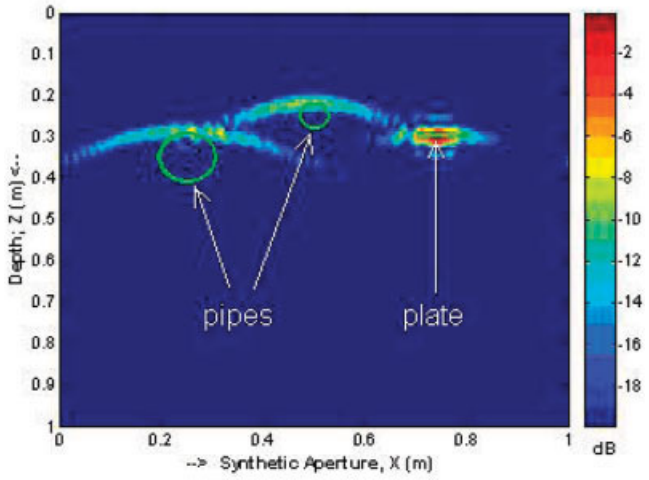

(b)

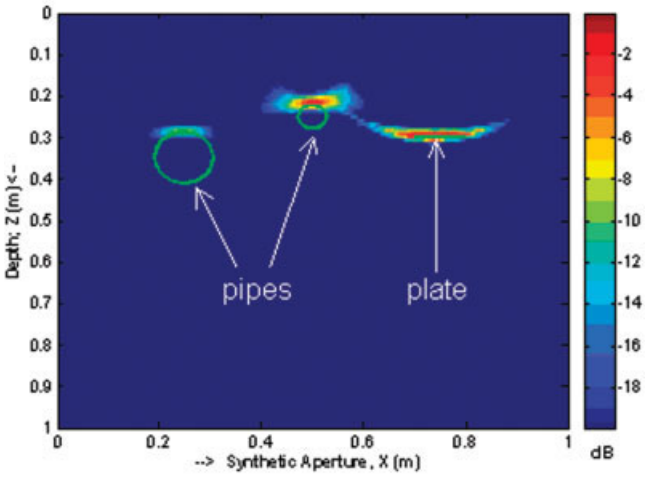

(c)

Figure 2 Simulated B-scan GPR images: (a) The CAD file of simulated objects; (b) Original defocused GPR image; (c) Focused GPR image after applying the proposed method. [Color figure can be viewed in the online issue, which is available at www.interscience.wiley.com]

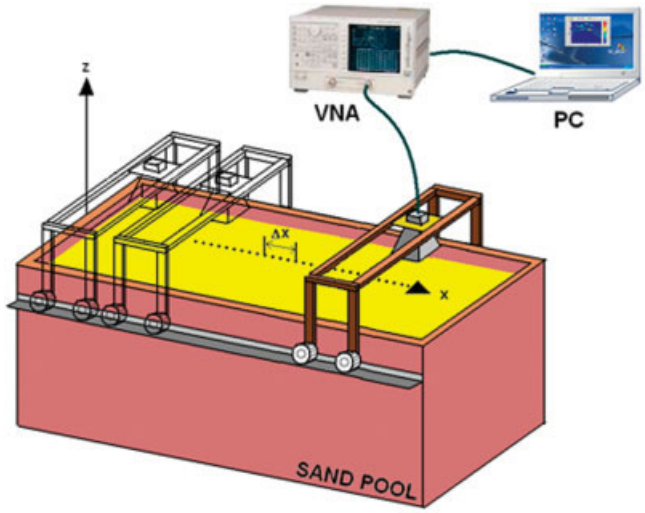

(a)

(b)

Figure 3 (a) Geometry of the B-scan GPR experimental set-up. (b) A scene from a monostatic measurement. [Color figure can be viewed in the online issue, which is available at www.interscience.wiley.com]

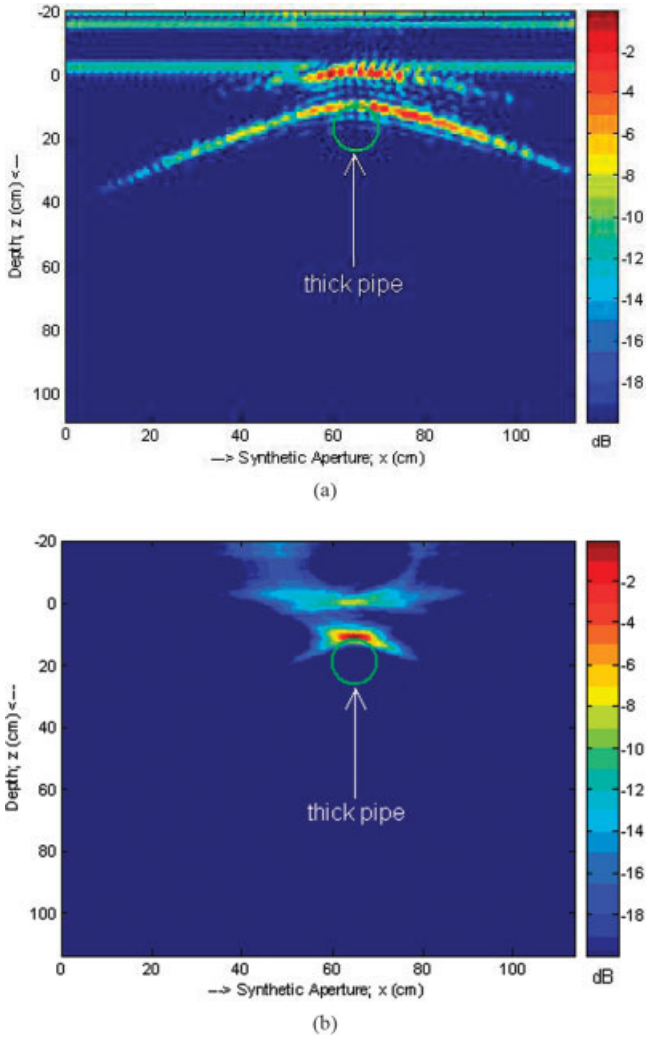

Figure 4 Measured B-scan GPR images for the monostatic case: (a) Hyperbolic image of a buried pipe; (b) Focused image after applying the proposed method. [Color figure can be viewed in the online issue, which is available at www.interscience.wiley.com]

As the second experiment, two metal pipes were buried at different locations. These identical pipes with 6 cm in diameter and 38 cm in length were buried horizontally at $x = 60$ cm and $z = 36$ cm, and at $x = 80$ cm and $z = 25$ cm. This time, we considered a bistatic configuration to mitigate the scattering from the sand's surface. Therefore, two C-band pyramidal rectangular horn antennas were put aside and just above the surface while collecting S_{21} measurements along a straight path of 120 cm with 61 discrete spatial points. This time, antennas were headed looking directly downward during the whole B-scan process. For each spatial point, the VNA's frequency is varied from 4.0 to 7.1 GHz with 15.5-MHz frequency steps to have 201 discrete frequency points. A 2-D B-scan GPR image is acquired as seen in Figure 5(a) by taking the 1-D IFT of the measured spatial-frequency data. Several observations can be made for the constructed GPR image: (i) Because of bistatic arrangement, the EM reflection from the air–sand surface is highly suppressed. This phenomenon can easily be seen from Figure 5(a) as the scattered energy from the surface barely falls within the -20 dB dynamic range of the display. (ii) Since most of the energy could penetrate inside the sand, thanks to bistatic configuration, we were able to sense the scattering from the bottom of the pool at $z = 63$ cm as well. This scattering occurs because of the impedance change between the sand and the bottom of the pool and is visible for the whole synthetic aperture of 120 cm. (iii) Scattering from the pipes becomes dominant in the image and experience the expected parabolic pattern. (iv) Scattering mechanism as the EM wave travels around the perimeter of the pipes can also be seen in the image as a result of new antenna arrangement. This mechanism showed up as weaker hyperbolas just under the main two hyperbolas. After applying our HS algorithm, we obtained the new GPR image as shown in Figure 5(b). It is obvious that this new image is more concentrated around the true location of the pipes and the reflections from other surfaces are well suppressed as they are not visible within the dynamic range of the figure. On the other hand, we also observe some image tails tending upwards from the true image location. This type of blurring is unavoidable in the present algorithm. This is because if the tails of the corresponding hyperbolic template pass over the true image location for the pixels that are located in upper regions, the energy within this hyperbolic template is summed to give some energy value although there is no scatterer present on this particular pixel location.

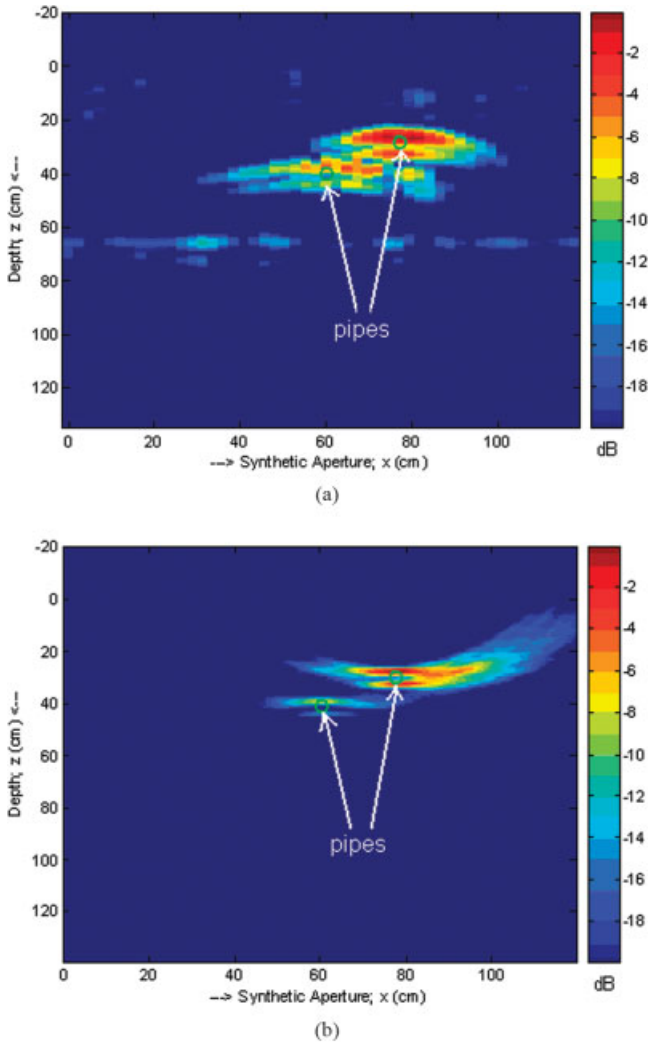

Figure 5 Measured B-scan GPR images for the bistatic case: (a) Hyperbolic image of two buried pipes; (b) Focused image after applying the proposed method. [Color figure can be viewed in the online issue, which is available at www.interscience.wiley.com]

4. DISCUSSIONS AND CONCLUSION

In this study, we presented and applied a focusing method based on hyperbolic summation (HS) technique to the simulated and measured B-scan GPR data generated via a SFR system, especially tested at C-band frequencies. The methodology was explained in detail and both numerical and measured examples, testing the effectiveness of the method, were presented. Application of the proposed method to the examples demonstrated that pipes and point scatterer-like objects produce very well-focused images in the new GPR image. This is due to the fact that the method uses hyperbolic templates corresponding to point-scatterers and converts these hyperbolas to single image pixels. The plate-like objects in the numerical examples also successfully produced well-focused images. In terms of computational efficiency, the algorithm is fast for 2-D B-scan images. It is clear that, the method can easily be adapted to 3-D C-scan images with hyperbolic surface templates. The method is examined with an SFR experimental set-up and measured B-scan GPR data. Both the traditional and the focused B-scan images were generated after applying the proposed method. Acceptable success has been achieved for the measured data as well.

The main weakness of the method becomes apparent for the case if any scattering mechanism falls under the hyperbolic template of another greater scattering, this point will produce a smaller scattering than its original EM energy in the final GPR image. Therefore, the energy levels in the final focused image will not correspond to the true energy levels of each scatterer. The other drawback of the method is that it produces ghost tails from the focused point toward upper regions as explained in Section 4. This phenomenon can be observed from Figure 5(b).

In this work, we only considered homogeneous and nearly lossless mediums. For inhomogeneous, lossy, and anisotropic mediums, the applicability of the method would be limited as the velocity and the wave number of the EM wave changes as the wave travels. Therefore, a model-based focusing method should be adopted for such soils.

ACKNOWLEDGMENTS

This work is supported by the Scientific and Research Council of Turkey (TUBITAK) under grant no. EEEAG-104E085. The authors are grateful to Mersin Trakya Cam A.Ş. for providing sand material and to Department of Mechanical Engineering of Mersin University for providing laboratory facilities for the conducted experiments.

REFERENCES

1. D.J. Daniels, Surface-penetrating radar, IEE Press, London, 1996.
2. L. Peters, Jr., D.J. Daniels, and J.D. Young, Ground penetrating radar as a subsurface environmental sensing tool, Proc IEEE 82 (1994), 1802–1822.
3. S. Vitebskiy, L. Carin, M.A. Ressler, and F.H. Le, Ultrawide-band, short pulse ground-penetrating radar: Simulation and measurement, IEEE Trans Geosci Remote Sens 35 (1997), 762–772.
4. L. Carin, N. Geng, M. McClure, J. Sichina, and L. Nguyen, Ultra-wide-band synthetic- aperture radar for mine-field detection, IEEE Trans Antennas Propag 41 (1999), 18–33.
5. J.I. Halman, K.A. Shubert, and G.T. Ruck, SAR processing of ground-penetrating radar data for buried UXO detection: Results from a surface-based system, IEEE Trans Antennas Propag 46 (1998), 1023–1027.
6. A. Sullivan, R. Damarla, N. Geng, Y. Dong, and L. Carin, Ultra wide-band synthetic aperture radar for detection of unexploded ordnance: Modeling and measurements, IEEE Trans Antennas Propag 48 (2000), 1306–1315.
7. C. Ozdemir, S. Lim, and H. Ling, A synthetic aperture algorithm for ground-penetrating radar imaging, Microwave Opt Tech Lett 42 (2004), 412–414.
8. E. Fisher, G.A. McMechan, A.P. Annan, and S.W. Cosway, Examples of reverse-time migration of single-channel, ground-penetrating radar profiles, Geophysics 57 (1992), 577–586.
9. L. Capineri, P. Grande, and J.A.G. Temple, Advanced image-processing technique for real-time interpretation of ground-penetrating radar images, Int J Imaging Syst Tech 9 (1998), 51–59.
10. C.J. Leuschen and R.G. Plumb, A matched-filter-based reverse-time migration algorithm for ground-penetrating radar data, IEEE Trans Geosci Remote Sens 39 (2001), 929–936.
11. I.L. Morrow and P.A. Van Genderen, 2D polarimetric backpropagation algorithm for ground-penetrating radar applications, Microwave Opt Technol Lett 28 (2001), 1–4.
12. O. Yilmaz, Seismic data processing, Society of Exploration Geophysicists, Tulsa, USA, 1987.
13. C. Cafforio, C. Prati, and F. Rocca, SAR data focusing using seismic migration techniques, Trans Aerospace Electron Syst 27 (1991), 194–206.
14. H. Ling, R. Chou, and S.W. Lee, Shooting and bouncing rays: Calculation the RCS of an arbitrary shaped cavity, IEEE Trans Antennas Propag 37 (1989), 194–205.
15. C. Ozdemir, R. Bhalla, L.C. Trintinalia, and H. Ling, ASAR—Antenna synthetic aperture radar imaging, IEEE Trans Antennas Propag 46 (1998), 1845–1852.
16. C. Ozdemir and H. Ling, ACSAR—Antenna coupling synthetic aperture radar imaging algorithm, J Electromagn Waves Appl 13 (1999), 285–306.

END-FED MODIFIED PLANAR DIPOLE ANTENNA FOR DTV SIGNAL RECEPTION

Yun-Wen Chi,[1] Kin-Lu Wong,[1] and Shih-Huang Yeh[2]

[1] Department of Electrical Engineering, National Sun Yat-Sen University, Kaohsiung 804, Taiwan

[2] Information and Communications Research Laboratories, Industrial Technology Research Institute, Hsinchu 310, Taiwan

Received 10 August 2006

ABSTRACT: *A novel end-fed modified planar dipole antenna for digital television (DTV) signal reception in the 470–806 MHz band is presented. The antenna is of a narrow rectangular shape (10 mm wide and 235 mm long) and is printed on a dielectric substrate. The antenna comprises a step-shaped radiating strip (arm 1) and a narrow rectangular radiating strip (arm 2), both separated by an L-shaped feed gap whose one open end located at the shorter edge or end edge of the antenna. Across this open end of the L-shaped feed gap, the antenna can be excited to provide a wide bandwidth (2.5:1 VSWR) of larger than 50%, which is much wider than that of a corresponding conventional center-fed dipole antenna and allows the proposed antenna easily cover the 470–806 MHz band for DTV signal reception. In addition, over the operating band, the radiation performance of the proposed antenna is similar to that of the conventional center-fed dipole antenna. The proposed end-fed modified planar dipole antenna is studied in detail in this paper.*

 Microwave Opt Technol Lett 49: 676–680, 2007; Published online in Wiley InterScience (www.interscience.wiley.com). DOI 10.1002/mop.22229

Key words: *antennas; DTV antennas; dipole antennas; printed antennas; broadband antennas*